

Study on the Uptake of Aqueous Zinc Ion Onto a Novel Organic Acid Modified Biosorbent

Chukwunonso O. Aniagor

Nnamdi Azikiwe University Faculty of Engineering Technology

D. M. Hussein

Sebha University

S. Farag

National Research Centre

Ali Hashem (✉ alhashem2000@yahoo.com)

National Research Centre <https://orcid.org/0000-0001-7981-4872>

Research Article

Keywords: Adsorption, Zinc ion, biosorbent, adsorption mechanism, adsorption modelling

Posted Date: June 18th, 2021

DOI: <https://doi.org/10.21203/rs.3.rs-456826/v1>

License:   This work is licensed under a Creative Commons Attribution 4.0 International License.

[Read Full License](#)

1 Study on the uptake of aqueous zinc ion onto a novel organic acid modified biosorbent

2 **Chukwunonso .O. Aniagor^{a*}, D. M. Hussein^b, S. Farag^c, A. Hashem^{c**}**

3
4 ^a*Department of Chemical Engineering, Nnamdi Azikiwe University, P.M.B. 5025, Awka, Nigeria.*

5 ^b*Chemistry Department, Faculty of Science, Sebha University, Sebha, Libya.*

6 ^c*Textile Research Division, National Research Centre, Dokki, Cairo, Egypt.*

7
8 ***Corresponding author:**

9 Email address: co.aniagor@unizik.edu.ng

10 Telephone no: +234-8061232153

11 ****Corresponding author:**

12 Email address: alihashem2000@yahoo.com

13 Telephone no: 00202-3371362 Ext. 2039

14 Fax: 00202-3370931

15 **ORCID**

16 *Chukwunonso O. Aniagor:* <http://orcid.org/0000-0001-6488-3998>

17 *A. Hashem:* <https://orcid.org/0000-0001-7981-4872>

18
19 **Abstract**

20 *Alhagi Graecorum (AG)* is an invasive plant with a massive/robust root structure that can grow
21 up to 12 feet into the ground. The present study exploited the rich cellulosic content in this
22 'AG' root for the synthesis of a novel biosorbent ('MA'). This low-cost biosorbent, with high
23 carboxyl content of 447.22 (m. eq /100 g sample) was utilised for aqueous zinc ion
24 sequestration. The surface functional groups and textural characteristics required for an
25 efficient heavy metal binding was identified on 'MA' using Fourier transform infrared
26 spectroscopy (FTIR) and scanning electron microscopy (SEM). Sip isotherm emerged as the
27 model of best fit for equilibrium studies, hence, Zn (II) ion sorption onto 'MA' is believed to
28 occur via a hybrid blend of homogenous monolayer and heterogeneous multilayer adsorption.
29 Meanwhile, the Elovich (SNE = 1.0429), intraparticle diffusion (SNE = 1.0205) and pseudo-

30 first-order (SNE = 1.0455) provided the best fitting for 200, 400 and 600 mg/L adsorption
31 system, respectively. The maximum adsorption capacity of 188.67 mg/g was recorded at
32 optimum adsorption conditions, with the predominance of the electrostatic and electron-donor-
33 acceptor interaction mechanism. The abundant surface oxygenous functional groups on 'MA'
34 positively influenced its adsorption capacity; thus, making it a promising biosorbent for
35 aqueous Zn (II) uptake.

36 **Keyword:** Adsorption; Zinc ion; biosorbent; adsorption mechanism; adsorption modelling

37 1. Introduction

38 Zn(II) is an essential element for healthy living when retained within the permissible
39 contamination limits (Jagaba *et al.*, 2020). A maximum permissible limit of 5 mg/L was
40 stipulated by the World Health Organization (WHO) and the United States Environmental
41 Protection Agency (USEPA) for Zn(II) in drinking water (Jagaba *et al.*, 2020). The existence
42 of Zn (II) ion above these stipulated limits could result in varying degrees of health challenges
43 (Barakat, 2011; Wołowiec *et al.*, 2019). Meanwhile, zinc ion contamination occurs mainly via
44 inappropriate disposal of chemical process industrial effluents into the aquatic environment
45 (Badruddoza *et al.*, 2013; Chen *et al.*, 2018) and their efficient removal pose a serious challenge
46 to researchers and the scientific community.

47 Several technologies (Awual, Hasan, Asiri, *et al.*, 2019; Badruddoza *et al.*, 2013; Matouq *et*
48 *al.*, 2015; Wołowiec *et al.*, 2019) have been applied for heavy metal uptake from an aqueous
49 environment. However, some of these technologies have associated limitations like low
50 treatment efficiency, high energy and cost requirement, non-eco-friendly, etc (Awual, 2016;
51 Awual, Hasan, Islam, *et al.*, 2019; Shahat, Hassan, Azzazy, *et al.*, 2018; Shahat, Hassan, El-
52 Shahat, *et al.*, 2018). In this work, the biosorption technique using a low-cost biosorbent
53 precursor was explored for the uptake of aqueous zinc ion. The preference for the biosorption

54 approach is related to its operational flexibility, process efficiency, efficient regeneration of
55 spent adsorbent, etc (Al-Shaalan *et al.*, 2019; Ali *et al.*, 2019; Ali *et al.*, 2018; Awual *et al.*,
56 2017). Consequently, a variety of biosorbents such as fungal mycelial wastes (Luef *et al.*,
57 1991), Rice bran (Wang *et al.*, 2006), *Azadirachta indica* bark (King *et al.*, 2008), immobilized
58 *Candida utilis* and *Candida tropicalis* cells (Ahmad *et al.*, 2013), rapeseed waste (Paduraru *et*
59 *al.*, 2015), have been successfully applied for aqueous zinc ion uptake. Also, the *Eichhornia*
60 *crassipes* biomasses were successfully applied for the uptake of copper ion (Abdelraheem *et*
61 *al.*, 2017; Abdelraheem *et al.*, 2016; Komy *et al.*, 2013). Meanwhile, the efficacy of a novel
62 biosorbent ('MA ') for zinc ion uptake was investigated in this study.

63 *Alhagi Graecorum* is an invasive tropical plant that often serves as animal fodder, but its
64 elimination from invaded farmland could be very challenging (Ebrahimi *et al.*, 2015).
65 Considering its invasiveness, relative availability and rich cellulosic content, *Alhagi*
66 *Graecorum* adoption as the choice of adsorbent precursor in this study is justified. Furthermore,
67 the novel biosorbent ('MA ') was obtained through dual reaction stages of direct carbonylation
68 of hydroxyl groups, – OH (using succinic acid) and subsequent esterification of the resultant
69 anhydride analogue into ester of high carboxyl (–COOH) content. The characteristics of the
70 biosorbent precursor and its modifier are complementary in certain ways. The *Alhagi*
71 *Graecorum* plant is readily available but with limited carboxyl groups availability, hence its
72 poor metal ion sorption capacity, while the esterification agent (succinic acid) is a liquid and
73 cannot be applied as a sole adsorbent. The aqueous zinc ion sorption ability of the novel
74 biosorbent was subsequently evaluated under batch mode. The surface chemistry, elemental
75 distribution and morphological features of the synthesized adsorbent were obtained, while the
76 effect of various process variable on the adsorption capacity was elucidated in the study.

77

78

79 2. Materials and methods

80 2.1. Materials

81 The *Alhagi Graecorum* (AG) plant was obtained from the Matrouh desert, Egypt. The root of
82 this plant was separated from the stems and leaves, and the latter was discarded. The root
83 material was carefully washed with distilled water to remove every adherent earth particle and
84 then oven-dried at 80 °C for 10 h. The dried root material was subsequent ground and sieving
85 to a particle size of 50–125 µm. All reagents used in this study; zinc acetate, EDTA, succinic
86 acid, acetic acid, sodium carbonate, acetone, and ethyl alcohol were all laboratory grade
87 chemicals, supplied by Merck, Germany.

88 2.2. Preparation of the adsorbent

89 The novel adsorbent (MA) was synthesized as follow; 2 g of the *Alhagi Graecorum* (AG)
90 powder was added to a beaker containing an aqueous solution of succinic acid whose volume
91 is sufficient enough to achieve a slurry. The mixture was manually stirred using a spatula to
92 achieve homogeneity. Afterwards, the homogeneous slurry was oven-dried (at 100–150 °C)
93 and subsequently cooled to room temperature to obtain 'MA'. The dried 'MA' sample was
94 washed with ethanol/water solution (80:20) to get rid of any unreacted acid/soluble by-
95 products, followed by oven-drying at 80 °C for 6 h.

96 2.3. Adsorbent characterization

97 2.3.1. Fourier Transform Infrared (FTIR) spectroscopy

98 To elucidate the inherent functional groups on the biosorbent precursor and the synthesized
99 biosorbent, the FTIR spectra studies were conducted. The IR spectra were recorded at the
100 wavelength range of 4000–400 cm⁻¹ using Perkin-Elmer, Shimadzu FTIR-8400S
101 spectrophotometer.

102 2.3.2. Scanning electron microscopy (SEM)

103 The surface morphologies of the adsorbent precursor, synthesized biosorbent and the spent
104 adsorbent were explained via SEM micrograph obtained using Scanning Electron Microscope,
105 Model JEOL-JSM-5600 (operating at accelerating voltage of 25.00 kV). During the analysis,
106 the respective biosorbent samples were placed on the microscope stub and coated with a thin
107 gold layer using a polaron diode sputter unit. Consequently, the energy dispersive X-ray (EDX)
108 mapping detector (Model JEOL-JSM-5600) attached to the SEM equipment was used for
109 studying the biosorbents' elemental distribution.

110 2.3.3. The pH at zero charge (pH_{pzc}) determination

111 The point of zero charge (pH_{pzc}) of the biosorbent was obtained following the procedure earlier
112 reported by Khalil *et al.* (1990) and Noh *et al.* (1990). In the procedure, the pH of 100 ml of
113 0.01N NaCl solution each contained in a separate conical flask was adjusted in the initial range
114 of pH 2.0 to pH 12.0, using a suitable volume of 0.01N HCl or 0.01N NaOH solution. After
115 noting the initial of the solution contained in the different conical flasks, about 0.1 g of the
116 biosorbent sample was introduced into each of the flasks followed by reaction for 24 h.
117 Subsequently, the final pH of the solutions in the different flasks was measured and recorded.
118 Then, the recorded initial pH values were plotted against the change in pH as shown in **Fig. 4a**

119 2.4. Carboxyl content estimation

120 0.2 g of the 'MA' was added to 50 mL of NaOH solution (0.03 N) contained in a conical flask.
121 The flasks and their content were allowed to equilibrate at 25 °C overnight. By titrating the
122 content of the flask with 0.01 N HCl solution. The carboxyl content of 'MA' was determined
123 via titration with 0.01 N HCl solution using phenolphthalein indicator (**Khalil *et al.*, 1990**) and
124 further evaluated using **Eq. (1)**.

125 $[\text{COOH}] \text{m. eq}/100\text{g. sample} = \frac{(V_0 - V_1)N}{W} \times 100$ (1)

126 Where V_0 = Volume of HCl consumed for the blank experiment (mL), V_1 = HCl volume (mL)
127 consumed by the adsorbent sample, N = normality of the HCl solution, and W = mass of the
128 'MA' (g).

129 2.5. Batch Adsorption Studies

130 A specific amount of 'MA' (0.03 g) was contacted with 100 mL of a Zn (II) ion solution in a
131 125 mL Erlenmeyer flask. The solution pH was rightly tuned using either 0.1 M HNO_3 or 0.1
132 M NaOH. After a certain period of agitation (at 150 rpm, 30 °C), the mixture was filtered using
133 Whatman No. 41 paper to separate the adsorbent and metal ion solution. The variation in the
134 Zn (II) ion concentration was obtained from the direct titration with a standard EDTA solution.
135 The effect of process variables on the 'MA' adsorption capacity was conducted by varying the
136 agitation time from 0 – 180 min, adsorbent mass from 0.3 – 7.0 g/L and adsorbate solution
137 temperature from 30 – 60 °C. Meanwhile, the relevant parameters (amount adsorbed at
138 equilibrium, q_e , and removal efficiency, R.E %) derivable from the adsorption experiment was
139 evaluated with **Eqs. (2) – (3)**. For the avoidance of experimental error, a duplicate version of
140 the respective batch adsorption and effect of process variable experiments were conducted and
141 the accurate mean values for q_e obtained in each case.

142 $q_e = \frac{(C_0 - C_e)V}{W}$ (2)

143 $\text{RE (\%)} = \frac{C_0 - C_e}{C_0} \cdot 100\%$ (3)

144 Where C_0 = Initial Zn (II) concentration (mg L^{-1}), C_e = Zn (II) concentration at equilibrium
145 (mg L^{-1}), W = adsorbent mass (g), V = volume of Zn (II) solution used (L).

146

147 2.6. Adsorption modelling

148 Insight into the adsorbate - adsorbent interaction during the adsorption process is obtained from
149 adsorption isotherm modelling, while the various model parameters could inform the probable
150 sorption mechanism (Abonyi *et al.*, 2019; Menkiti, Abonyi, *et al.*, 2018; Vargas *et al.*, 2012).
151 The experimental equilibrium data generated from this study were modelled with nonlinear
152 form of Langmuir (Hashem *et al.*, 2016; Hashem, Badawy, *et al.*, 2020; Langmuir, 1916),
153 Freundlich (Freundlich, 1907; Ighalo *et al.*, 2020; Igwegbe, Onukwuli, *et al.*, 2020), Temkin
154 (Menkiti, Aniagor, *et al.*, 2018; Temkin, 1940), D-R (Foo *et al.*, 2010; Hashem, Nasr, *et al.*,
155 2020), Khan (ANIAGOR *et al.*, 2020; Khan *et al.*, 1997), Redlich-Peterson (Menkiti &
156 Aniagor, 2018; Redlich *et al.*, 1959), Toth (Schweitzer *et al.*, 2018; Toth, 1971) and Sips
157 (ANIAGOR *et al.*, 2020; Yan *et al.*, 2019) models. The mathematical expression of these
158 isotherm models is presented in Table 1. Similarly, the dynamics and kinetics involved in the
159 present sorption process were studied using pseudo-first-order (Aniagor *et al.*, 2018; Hashem
160 *et al.*, 2015), pseudo-second-order (Aniagor *et al.*, 2019; Hashem *et al.*, 2011), Elovich
161 (Menkiti, Aniagor, *et al.*, 2018), intraparticle diffusion (Hashem, Fletcher, *et al.*, 2020;
162 Menkiti, Abonyi, *et al.*, 2018) and Bangham (Aniagor *et al.*, 2018) kinetic models. The kinetic
163 model equations are also presented in **Table 2**.

164 The nonlinear model goodness of data fit is usually evaluated from the magnitude of some
165 dedicated goodness-of-fit (GO-Fm) models. The goodness of fit evaluation is made based on
166 the following criteria: (i) the lower the error values for a given isotherm or kinetic model, the
167 better the model fit, (ii) the larger the R²-value the better the model fit. The GO-Fm models
168 applied in this work comprised of average relative error, ARE (Marquardt, 1963), average
169 percentage error, APE (Khair *et al.*, 2017), the sum of squared error, SSE (Ng *et al.*, 2002),
170 hybrid fraction error, HYBRID (Kapoor *et al.*, 1989), Marquardt's Percent Standard Deviation,
171 MPSD (Marquardt, 1963), Nonlinear chi-square test, χ^2 (Rivas *et al.*, 2006) and Coefficient of

172 determination, R^2 (Kumar *et al.*, 2008). The equation of these GO-Fm models is presented in

173 **Table 3.**

174 **Table 1:** The isotherm model equations applied in the study

2-parameter models		3-parameter models	
Model name	Model Equation	Model name	Model Equation
Langmuir	$q_e = \frac{q_m k_L C_e}{1 + k_L C_e}$	Khan	$q_e = \frac{q_{mK} * b_K * C_e}{(1 + b_K * C_e)^{a_K}}$
Freundlich	$q_e = K_F (C_e)^{\frac{1}{n_F}}$	R-P*	$q_e = \frac{A_{RP} C_e}{1 + B_{RP} * (C_e)^g}$
Tempkin	$q_e = \frac{RT}{b_T} \ln(K_T C_e)$	Sip	$q_e = \frac{K_s * C_e^{\beta_1}}{1 + a_s * C_e^{\beta_1}}$
D-R*	$q_e = q_D * \exp \left\{ -B_D \left[RT \left(1 + \frac{1}{C_e} \right) \right]^2 \right\}$	Toth	$q_e = \frac{k_T * C_e}{(a_T + C_e)^{t-1}}$

175 *D-R = Dubinin–Radushkevich ; R-P = Redlich-Peterson

176

177

178 **Table 2:** The kinetic model equations applied in the study

Model name	Model equation
Pseudo-first-order	$q_t = q_e [1 - \exp(-k_1 t)]$
Pseudo-second-order	$q_t = \frac{k_2 * q_e^2 * t}{(1 + k_2 * t)}$
Bangham	$q_t = q_e [1 - \exp(-k_b t^n)]$
Elovich	$q_t = \beta * \ln(\alpha \beta t)$
Intraparticle diffusion	$q_t = k_{id} t^{0.5}$

179

180

181

182 **Table 3:** The applied goodness-of-fit models

Error Function	Equation
Average Relative Error (ARE)	$ARE = \sum_{i=1}^n \left \frac{(q_e)_{\text{exp.}} - (q_e)_{\text{calc.}}}{(q_e)_{\text{exp.}}} \right $
Average Percentage Error (APE)	$APE\% = \frac{\sum_{i=1}^N [(q_e)_{\text{exp.}} - (q_e)_{\text{calc.}} / q_{\text{exp.}}]}{N} \times 100$
Sum Squares Error (ERRSQ/SSE)	$ERRSQ = \sum_{i=1}^n [(q_e)_{\text{calc.}} - (q_e)_{\text{exp.}}]^2$
Hybrid Fraction Error Function (Hybrid)	$Hybrid = \frac{100}{n-p} \sum_{i=1}^n \left[\frac{((q_e)_{\text{exp.}} - (q_e)_{\text{calc.}})^2}{(q_e)_{\text{exp.}}} \right]_i$
Marquardt's Percent Standard Deviation (MPSD)	$MPSD = \left(100 \sqrt{\frac{1}{n-p} \sum_{i=1}^n \left[\frac{((q_e)_{\text{exp.}} - (q_e)_{\text{calc.}})^2}{(q_e)_{\text{exp.}}} \right]} \right)^2$
Nonlinear chi-square test (χ^2)	$\chi^2 = \sum \frac{(q_{e,\text{exp}} - q_{e,\text{theoretical}})^2}{q_{e,\text{theoretical}}}$
Coefficient of determination (R^2)	$R^2 = \frac{\sum_{i=1}^n (q_{e,\text{calc}} - \overline{q_{e,\text{exp}}})^2}{\sum_{i=1}^n (q_{e,\text{calc}} - \overline{q_{e,\text{exp}}})^2 + \sum_{i=1}^n (q_{e,\text{calc}} - q_{e,\text{exp}})^2}$

183

184 3. Results and discussion

185 3.1. Reaction mechanisms involved during adsorbent synthesis

186 The novel adsorbent ('MA') was synthesized following the procedure presented in **section 2.2**
 187 and the reaction mechanism involved during the synthesis process is elucidated herein. The
 188 heat treatment involved during the oven-drying of the succinic acid impregnated *Alhagi*
 189 *Graecorum* powdered (AG) catalysed the direct carbonylation of the succinic acid to its
 190 corresponding anhydride according to **Eq. (4)**. The acid anhydride groups further reacted with
 191 the hydroxyl groups of 'AG' (Cell-OH) via partial or complete esterification to produce mono-

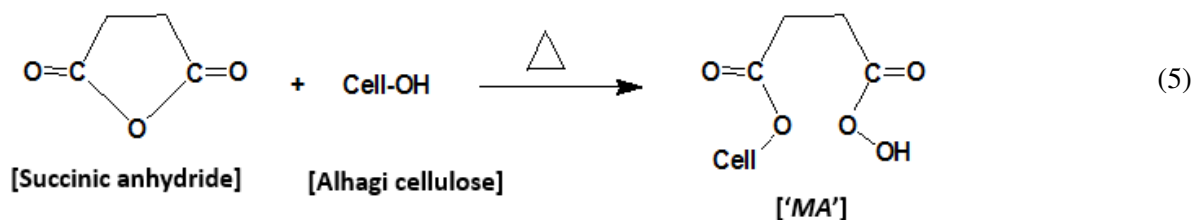
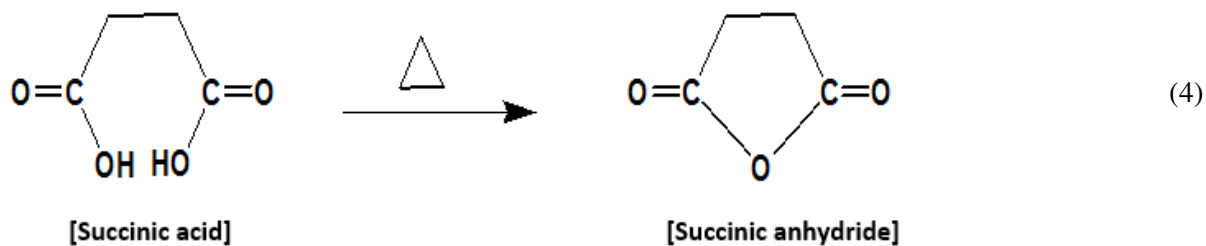
192 or di-ester, respectively of high carboxyl content, which is the desired novel adsorbent ('MA')

193 [as shown in Eq. (5)]. The carboxyl content of the synthesized 'MA', as evaluated from Eq. (1)

194 is 447.22 (m. eq /100 g sample) at optimum reaction conditions. The factors that affected the

195 carboxyl yield during the biosorbent synthesis is further discussed in subsection 3.1.1.

196



200 3.1.1. Effect of adsorbent synthesis process variables

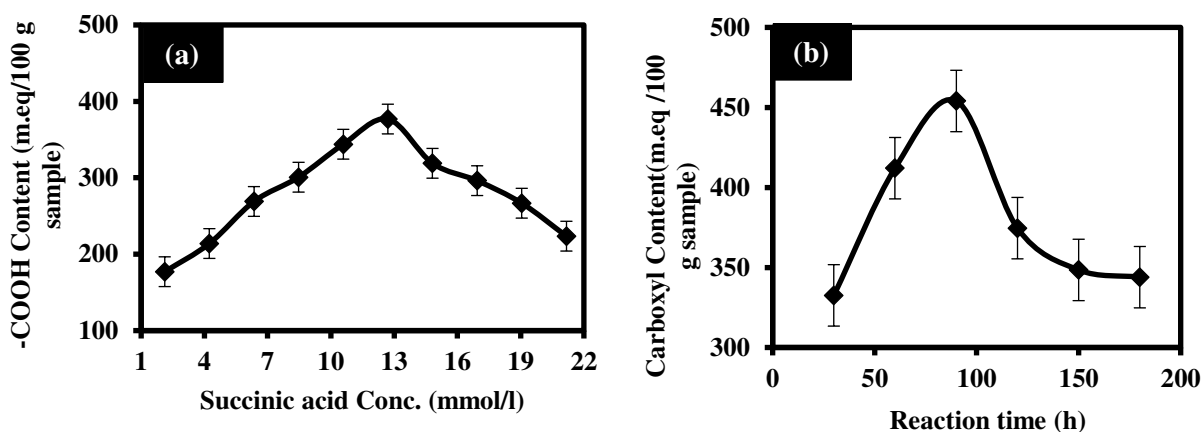
201 ***Effect of succinic acid concentration***

202 The variation of the succinic acid concentration and the biosorbents' carboxyl content is shown
203 in Fig. 1 (a). The –OH groups of the biosorbent precursor are considered as the limiting reactant
204 during the synthesis process. Therefore, the more readily the organic acid groups reach and
205 interact with them, the more carboxyl group formation. This could be the reason for the
206 observed increment in the carboxyl content on the 'MA' the succinic acid concentration initially
207 increased (see Fig. 1a). Meanwhile, at much higher acid concentrations, the unavailability or
208 probable exhaustion of formally available hydroxyl groups of the precursor material may cause
209 the dissociation of already existent carboxyl groups, thus the observed carboxyl content
210 reduction (Fig. 1a).

211 ***Effect of dehydration time***

212 The variation of the succinic acid concentration and the biosorbents' carboxyl content is shown
213 in Fig. 1(b). The plot depicted a sustained increment in 'MA' carboxyl content with dehydration
214 time up to 90 h, however, further extension of the dehydration time (beyond 90 h) caused a
215 decline. Accordingly, during the initial increase in dehydration time (from 30 h to 90 h), there
216 was adequate predisposal time for achieving an optimal esterification reaction between the
217 hydroxyl groups of the cellulosic biomass and the anhydride analogue of the succinic acid.
218 However, as the dehydration time extended beyond 90 h, there was the exhaustion of the
219 esterification sites, hence the observed decline in carboxyl content.

220



221

222 **Fig. 1:** The effect of (a) Succinic acid concentration and (b) dehydration time on the carboxyl
 223 content of 'MA' (error bars represent \pm standard experimental errors)

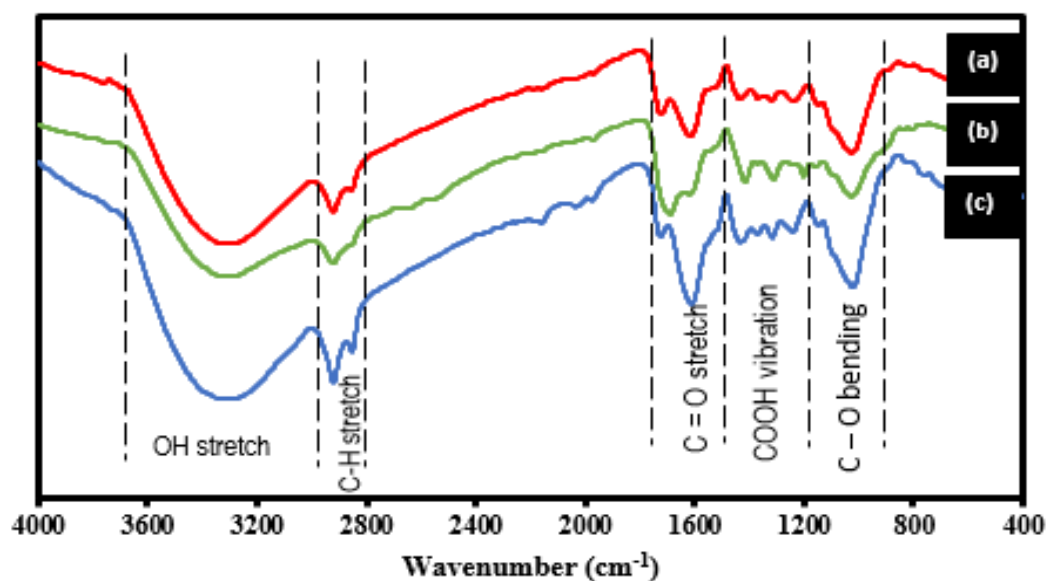
224

225 3.2. Adsorbent characterization

226 3.2.1. Fourier transform infrared spectroscopy (FTIR)

227 The FTIR spectra of the raw (AG), modified (MA) and metal loaded [Zn (II)-MA] biosorbent
 228 together with their observed peaks are presented in **Fig. 2**. Similar peaks were observed for the
 229 biosorbent samples, except for some slight wavenumber shifts, peak broadening or shrinking
 230 etc sequel to functionalization and heavy metal loading. The prominent peaks identified at 3333
 231 cm^{-1} , 2916 cm^{-1} , 2844 cm^{-1} , between 1719 & 1610 cm^{-1} , and the one around 1512 cm^{-1} is
 232 assigned to the O–H stretching vibration, symmetric C–H stretch, asymmetric C–H stretch,
 233 aromatic C=O group of ester and lignin C-O linkage, respectively (Adigun *et al.*, 2019). The
 234 peaks domicile at 1423 and 1228 cm^{-1} are typical of the asymmetric –COOH stretch of cellulose
 235 and hemicellulose. Also, a signature bending vibration band of the C–O group is assigned to
 236 the peak at wavenumber 1024 cm^{-1} (Sasmal *et al.*, 2012). Meanwhile, the post adsorption FTIR
 237 pattern is characterized by variations in peak length and intensities (**Fig. 2**).

238



239

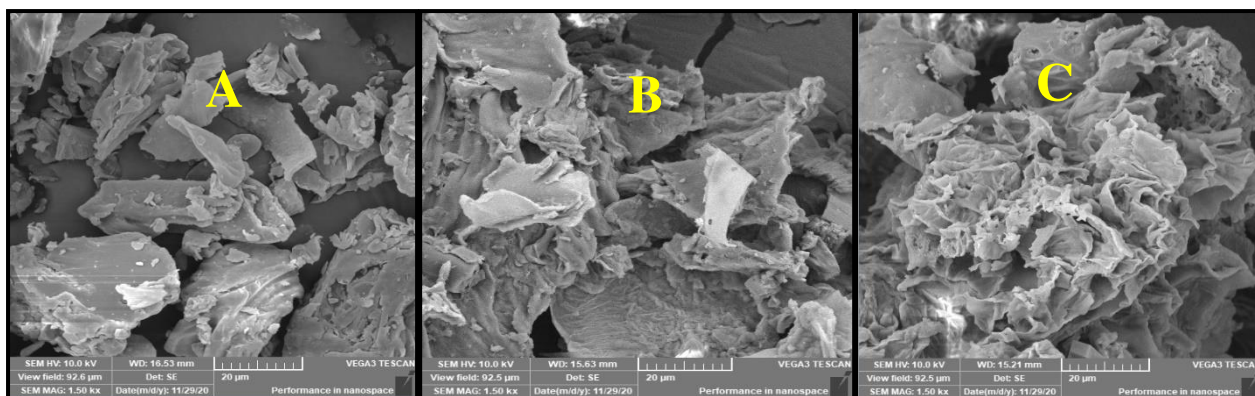
240

Fig. 2: FTIR spectra for (a) Zn (II) Loaded 'MA' (b) 'MA' (c) Raw Alhagi

241 3.2.2. Scanning electron microscopy (SEM)

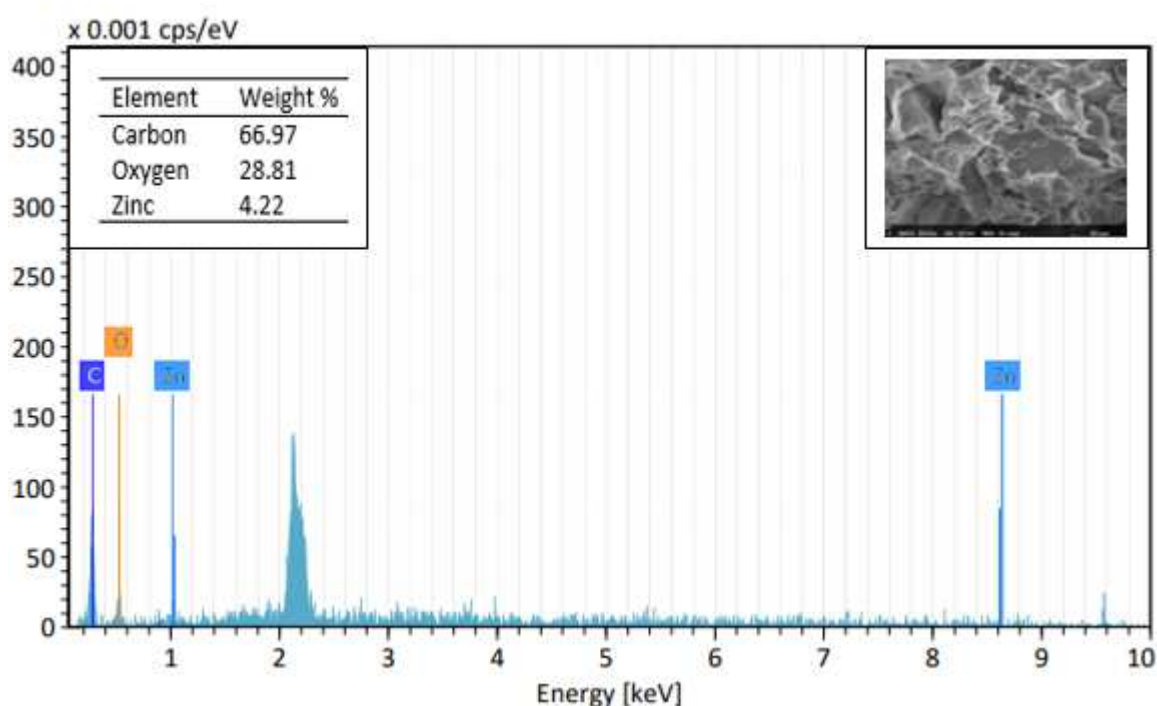
242 The raw Alhagi (**Fig. 3a**) depicted a textural characteristic of thin, paper-like overlapped
 243 structures, with some degree of surface roughness and poorly developed pores. After
 244 undergoing the functionalization stages of acid and heat treatment, 'MA' surface significantly
 245 transformed and depicted well-developed pores and increased surface roughness (**Fig.3b**).
 246 Upon further comparison of the pre-and-post adsorption image of MA (**Figs. 3b & 3c**), the
 247 only obvious identified distinction is that the surface of Zn (II)-loaded 'MA' depicted a
 248 characteristic lustre. This could probably be due to the presence of the adsorbed zinc ion.

249 The EDX elemental mapping was performed to confirming the presence of adsorbed zinc ions
 250 and also to ascertain their percentage deposition. As shown in **Fig. 4**, the presence of carbon
 251 (66.97 %), oxygen (28.81 %) and Zinc (4.22 %) was detected in the post adsorption 'MA'
 252 sample. This finding serves as a confirmation for the uptake of Zinc ion by 'MA' via the
 253 adsorption process.



254

255 **Fig. 3:** SEM images of (a) raw Alhagi (b) 'MA' (c) Zn (II)-loaded 'MA'



256

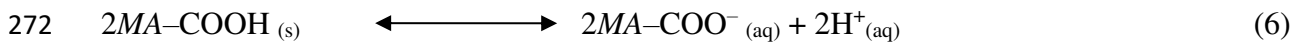
257 **Fig. 4:** EDX spectra for Zn (II)-loaded 'MA'

258 3.3. Adsorption performance of 'MA'

259 3.3.1. Effect of pH

260 It has been reported that the surface charge of a given adsorbent is a function of the adsorbate
 261 solution pH and its (biosorbents') point of zero charges, pH_{PZC} . According to **Fig. 5a**, the 'MA'
 262 depicted a pH_{PZC} of pH 4.1, an indication of its surface acidity nature. The assertion was further

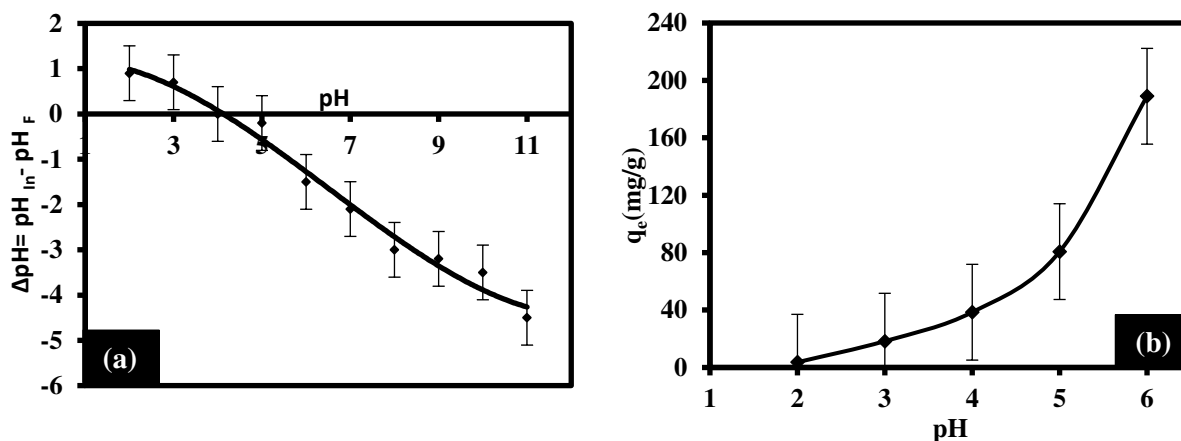
263 corroborated by the presence of carboxylic functional groups identified from the FTIR spectra.
 264 Meanwhile, **Eqs. (6)** and **(7)** presents the stoichiometric illustration of the ion
 265 exchange/electrostatic interaction mechanism occurring within the zinc ion sorption system.
 266 These equilibrium reactions are strongly dependent on the pH of the adsorbate solution. At
 267 strongly acidic conditions ($\text{pH} < \text{pH}_{\text{PZC}}$) the backward reaction of Eq (6) is favoured, thus the
 268 predominance of the carboxylic groups on the adsorbent in its non-ionized form. A typical
 269 scenario was observed at pH 2.0 (Figure 5b), where no notable adsorption capacity value was
 270 recorded, due to a strong electrostatic repulsion between the zinc cations and protonated
 271 adsorbent surfaces.



273



275 Subsequent deprotonation of the adsorption sites as shown in Eq. (7) due to a decrease in the
 276 acidity of the adsorption system ($\text{pH} > \text{pH}_{\text{pzc}}$) greatly improved the adsorbents' adsorption
 277 capacity. For instance, the adsorption capacity was raised from 0 to 18.34 mg/g just by a single
 278 unit increase in the solution pH (from pH 2.0 to pH 3.0). Subsequent and progressive single
 279 unit-wise increase in the solution pH close to and beyond the pH_{pzc} always resulted in more
 280 than 50 % improvement in the adsorption capacity until the attainment of a maximum at pH
 281 6.0 (optimum pH for the study). Notably, the pH variation studies were terminated at pH 6.0,
 282 as the author had initially recorded insignificant adsorption at alkaline pH regions due to
 283 possible precipitation of the zinc cation to its hydroxide analogue.



284

285 **Fig. 5:** Plot of the (a) pH of point of zero charge (b) effect of pH on the adsorption capacity

286 (error bars represent \pm standard experimental errors)

287

288 3.3.2. Effect of adsorbent dosage

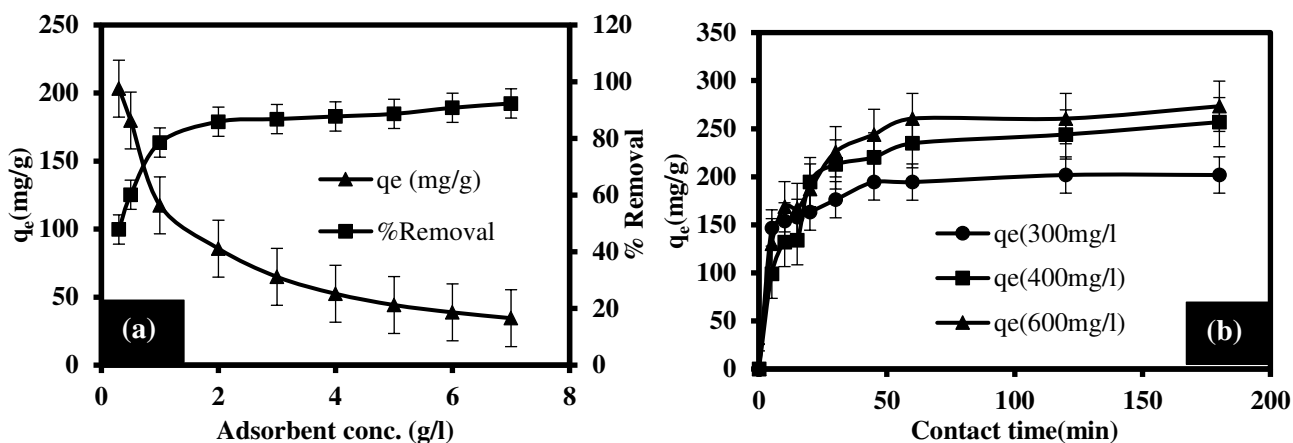
289 The variation in the adsorption capacity (mg/g) and removal efficiency (%) of 'MA' due to the
 290 amount of adsorbent used (dosage, g/L) was simultaneously investigated. According to the
 291 result presented in **Figure 6a**, the adsorption capacity was found to vary inversely as the
 292 removal efficiency. Meanwhile, Igwegbe, Oba, *et al.* (2020) has reported the strong
 293 dependence of removal efficiency on the adsorbates' initial concentration, hence, their values
 294 may not provide an accurate reflection of the sorption ability of a given adsorbent. Therefore,
 295 our discussion here only emphasized the relationship between that adsorbent dosage and
 296 adsorption capacity (which provides a better reflection of the adsorbents' intrinsic adequacy)
 297 (Aniagor *et al.*, 2021; Igwegbe, Oba, *et al.*, 2020; Oba *et al.*, 2021).

298 Figure 6a generally depicted a steady decline in the adsorption capacity as the adsorbent dosage
 299 increased from 0.3 to 7.0 g/L. Although a general decline in the adsorption capacity was
 300 observed as the adsorbent dosage increased, however, the extent of adsorption capacity decline
 301 is particularly dependent on the adsorbent mass ratio at a given time. For instance, a 0.2 g/L
 302 increased in the adsorbent dosage (that is from 0.3 to 0.5 g/L) resulted in about a 12 % loss of

303 adsorption capacity, while a 0.5 g/L increase (that is from 0.5 to 1.0 g/L) showed about 35 %
304 adsorption capacity loss. A similar observation which is related to the progressive saturation
305 and eventual clogging of the adsorption sites, thus limiting zinc ions adsorption, were made at
306 higher adsorbent dosages (Hashem, ANIAGOR, Nasr, *et al.*, 2021; Hashem, Badawy, *et al.*,
307 2020). Hence, the maximum adsorption capacity for the study was recorded at 0.3 g/L
308 adsorbent dosage.

309 3.3.3. Effect of adsorption time

310 Figure 6b presents the combined plot of contact time and initial concentration effect on the
311 adsorption capacity. The amount adsorbed generally improved as the adsorption time extended
312 and as the initial adsorbate concentration increased. Meanwhile, a rapid uptake was witnessed
313 within the first 10 min of adsorption, as the respective amount of zinc ion adsorbed was strongly
314 dependent on the initial adsorbate concentration. Within this initial adsorption stage (first 10
315 min), about 80 % of the optimum adsorption capacity for the study was realized. This
316 occurrence could be due to the huge availability of active sites and the high solute (zinc ion)
317 concentration gradient which offered a substantial driving force for favourable uptake (Zhuang
318 *et al.*, 2019; Zhuang *et al.*, 2020). As the adsorption time extended (beyond 10 min), the solute
319 uptake amounts progressively diminished until the attainment of equilibrium at 120 min. The
320 adsorption capacity reduction as contact time extended is due to the progressive saturation of
321 the adsorption sites, thus limiting the uptake of more solutes (Guo *et al.*, 2019). Similar
322 equilibrium time as that obtained in this study has been previously reported by other authors
323 that employed cellulose-based adsorbent in the uptake of different metal cations (Ebrahimi *et*
324 *al.*, 2015; Hashem, Badawy, *et al.*, 2020; Hashem, Fletcher, *et al.*, 2020).



325
 326 **Fig. 6:** (a) Combined effect of adsorbent dose on adsorption capacity and removal efficiency (b)
 327 effect of contact time on the adsorption capacity at varying initial adsorbate concentration (*error bars*
 328 *represent \pm standard experimental errors*)

329 3.4. Adsorption modelling

330 3.4.1. Isotherm studies

331 The adsorbate concentration effect of the equilibrium adsorption data was fitted to different
 332 isotherm models whose equations are depicted in **Table 1**. The evaluated model parameters
 333 and their R^2 -values are presented in **Table 4**, while the experimental dataset was presented as
 334 a plot in **Fig. 7**. Meanwhile, the insufficiency of the application R^2 -value alone for the
 335 determination of the best fit nonlinear model has been highlighted (Abonyi *et al.*, 2019). As a
 336 result, seven (7) error model, whose equations are presented in **Table 3** were applied for
 337 determining the best-fit isotherm model. To limit the inconsistencies often experienced during
 338 the application of multiple error model (as was the case in this study), a process of normalizing
 339 the different error values from the error models for a given isotherm was adopted.
 340 Consequently, only the sum of normalized error (SNE) value will be considered during the
 341 isotherm modelling discussion and the lower the SNE value (as shown in **Table 5**), the better
 342 the model fit to the experimental isotherm data. The error values and the corresponding SNE
 343 for all the isotherm models are depicted in **Table 5**.

344 The Sips model is considered the overall best fit since it returned the lowest SNE value of
345 1.0498 and an appreciably high R²-value. As a hybrid model, Sip isotherm bridges between the
346 homogenous monolayer and heterogeneous multilayer postulations of the Langmuir and
347 Freundlich model, respectively. At low adsorbate concentration, the Sip model tilt towards the
348 Freundlich model and conversely favour the Langmuir model at high concentration. The
349 Freundlich constant 'n' (adsorbate-adsorbent affinity index) value which is greater than unity
350 indicates favourable adsorption (Liu *et al.*, 2018), which occurred mostly at low adsorbate
351 concentration.

352 The magnitude of the D-R mean energy (E, KJ/mol) is often applied for classifying the nature
353 of a given adsorption system (Hashem, Aniagor, Hussein, *et al.*, 2021). The physical and
354 chemical nature of an adsorption system is respectively implied at E < 8 KJ/mol and E > 8
355 KJ/mol (Dada *et al.*, 2012). By applying Eq. (8), a D-R mean energy value of 0.382 KJ/mol (E
356 < 8 KJ/mol) was obtained in the study. Hence, the occurrence of physical adsorption, with
357 electrostatic interaction between the adsorbate and adsorbent, which was further confirmed in
358 section 3.7, is thus postulated (Wang *et al.*, 2013).

$$359 \quad E = \frac{1}{\sqrt{2\beta_D}} \quad (8)$$

360 The Langmuir model also showed a maximum adsorption capacity of 229.985 mg/g and sa
361 favourability index (R_L) of 7.0E-03, which is indicative of a favourable adsorption process.
362 The positive Temkin isotherm constant (b_T) recorded in the study implies a favourable sorption
363 process. Furthermore, the heterogeneity of the Zinc adsorption system was further confirmed
364 by the Redlich-Peterson g-values of 0.195, which is approaching zero. Judging from the SNE
365 values, the best-fitted adsorption isotherm models in their descending order is Sips > Toth >
366 Redlich–Peterson > Khan > Freundlich > Temkin > Langmuir > Dubinin–Radushkevich.
367

368 **Table 4:** Isotherm model parameters

2-parameter models			
Langmuir	Freundlich	Temkin	D-R*
$q_{\max} = 229.985$	$n_F = 3.109$	$A_T = 7.6E-02$	$q_o = 182.656$
$K_L = 1.6134$	$K_F = 23.371$	$b_T = 52.219$	$B_0 = 1.3E-03$
$R_L = 7.0E-03$	$R^2 = 0.983$	$R^2 = 0.987$	$R^2 = 0.993$
$R^2 = 0.990$			
3-parameter models			
Khan	R-P*	Sips	Toth
$q_{\max} = 2.125$	$k_g = 29.109$	$K_S = 4.970$	$k_T = 13.592$
$b_K = 303.079$	$\alpha_R = -0.127$	$\alpha_S = 6.1E-03$	$\alpha_T = 9.0E-02$
$\alpha_K = 0.633$	$g = 0.195$	$\beta_S = 0.600$	$1/t = 0.588$
$R^2 = 0.982$	$R^2 = 0.981$	$R^2 = 0.971$	$R^2 = 0.981$

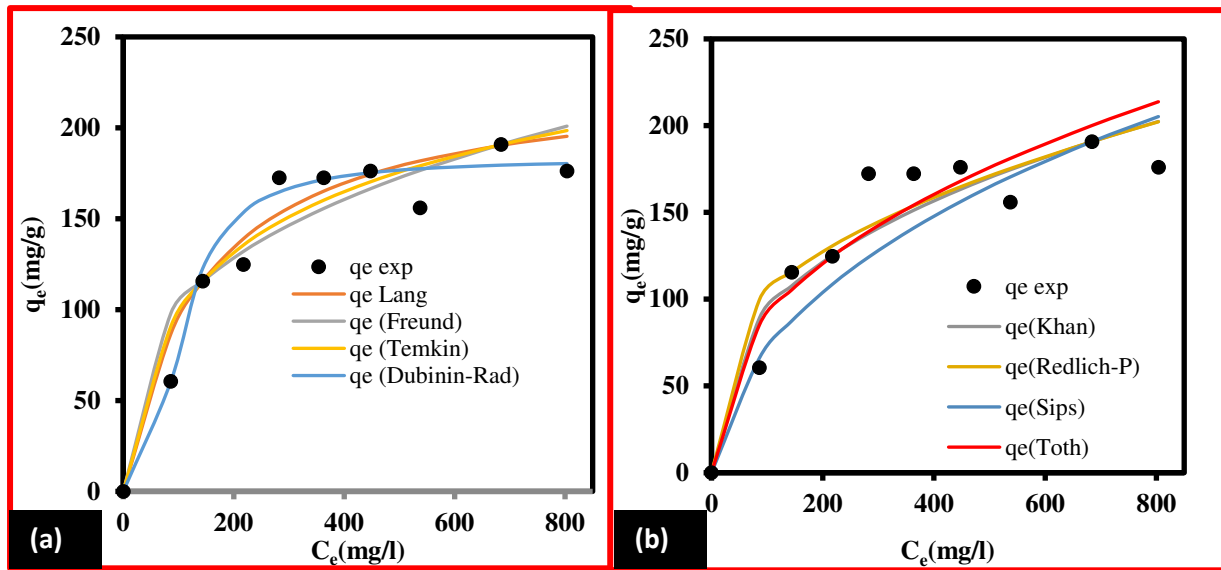
369 *D-R = Dubinin–Radushkevich; R-P = Redlich-Peterson

370

371 **Table 5:** Error-values for isotherm modelling

2-parameter models			
Langmuir	Freundlich	Temkin	D-R*
ARE = 0.988	ARE = 1.269	ARE = 1.107	ARE = 0.568
APE = 10.976	APE = 14.104	APE = 12.304	APE = 6.309
EABS = 114.377	EABS = 145.447	EABS = 129.053	EABS = 82.404
ERRSQ = 2360.033	ERRSQ = 3706.172	ERRSQ = 2846.789	ERRSQ = 1541.017
Hybrid = 21.817	Hybrid = 36.821	Hybrid = 26.851	Hybrid = 11.103
MPSD = 0.253	MPSD = 0.464	MPSD = 0.321	MPSD = 0.082
X ² = 17.735	X ² = 28.374	X ² = 0.21.607	X ² = 9.552
SNE = 1.0704	SNE = 1.0611	SNE = 1.0672	SNE = 1.0714
3-parameter models			
Khan	R-P*	Sips	Toth
ARE = 1.211	ARE = 1.319	ARE = 1.300	ARE = 1.267
APE = 13.452	APE = 14.653	APE = 14.443	APE = 14.081
EABS = 150.677	EABS = 151.446	EABS = 193.301	EABS = 167.086
ERRSQ = 3734.883	ERRSQ = 4047.317	ERRSQ = 5864.111	ERRSQ = 4377.627
Hybrid = 30.715	Hybrid = 40.132	Hybrid = 37.165	Hybrid = 32.363
MPSD = 0.325	MPSD = 0.506	MPSD = 0.245	MPSD = 0.299
X ² = 27.857	X ² = 30.868	X ² = 45.670	X ² = 29.358
SNE = 1.0600	SNE = 1.0590	SNE = 1.0498	SNE = 1.0558

372 *D-R = Dubinin–Radushkevich; R-P = Redlich–Peterson



374 **Fig. 7:** The isotherm plot for (a) 2-parameter models (b) 3-parameter model

375 3.4.2. Kinetic studies

376 As already explained in **section 3.4.1**, only the sum of normalized error (SNE) value will be
 377 considered in the discussions on kinetic studies and the lower the SNE value (as shown in
 378 **Table 6**), the better the kinetic model fit. The error values and the corresponding SNE values
 379 for all the kinetic models are depicted in **Table 6**. The Elovich (SNE = 1.0429), intraparticle
 380 diffusion (SNE = 1.0205) and pseudo-first-order (SNE = 1.0455) provided the best fitting for
 381 200, 400 and 600 mg/L adsorption system, respectively. Similarly, the plot of the different
 382 kinetic models is presented in **Fig. 8**.

383 Despite the emergence of the respective best fit models, the relatively low SNE value (\leq
 384 1.0872) and high R^2 -values (≥ 0.92) recorded for all models applied in modelling of the entire
 385 adsorption system (200, 400 and 600 mg/L) shows their good fitting to the experimental
 386 dataset. Studies (Delgado *et al.*, 2019; Wang *et al.*, 2020) have shown that PFO usually
 387 provides a better fit at high initial adsorbate concentration, where the ratio of adsorbate ions is
 388 higher compared to the available active sites. This assertion supports the emergence of PFO as
 389 the best fit model for the 600 mg/L adsorption system. Meanwhile, the linear dependence of its

390 rate constant (k_1) on the initial Zn (II) ion concentration has been highlighted (Wang *et al.*,
391 2020). The values of adsorption rate constant recorded for the PFO model (which ranges from
392 0.0683 to 0.155) (**Table 7**) was in all cases greater than those obtained for PSO; thus,
393 emphasizing the superiority of PFO model prediction to that of PSO in this study. Elovich
394 model postulates the heterogeneity of an adsorbents' surface and a direct variation between the
395 adsorption duration and activation energy (Aniagor *et al.*, 2019). The model also depicted a
396 low desorption constant (β) value in the range of 0.020 - 0.024 (**Table 7**), which implies
397 improved zinc ion sorption onto 'MA' for all adsorption systems. Notably, the value of
398 intraparticle (c-value) recorded for the 400 mg/L system was extraordinarily low (0.01) and it
399 implies a negligible boundary layer effect within such a system. Conversely, the occurrence of
400 greater boundary layer effects was observed for 200 and 600 mg/L adsorption system, as
401 informed by their large c-values of 134.767 and 131.564, respectively (**Table 7**).

402

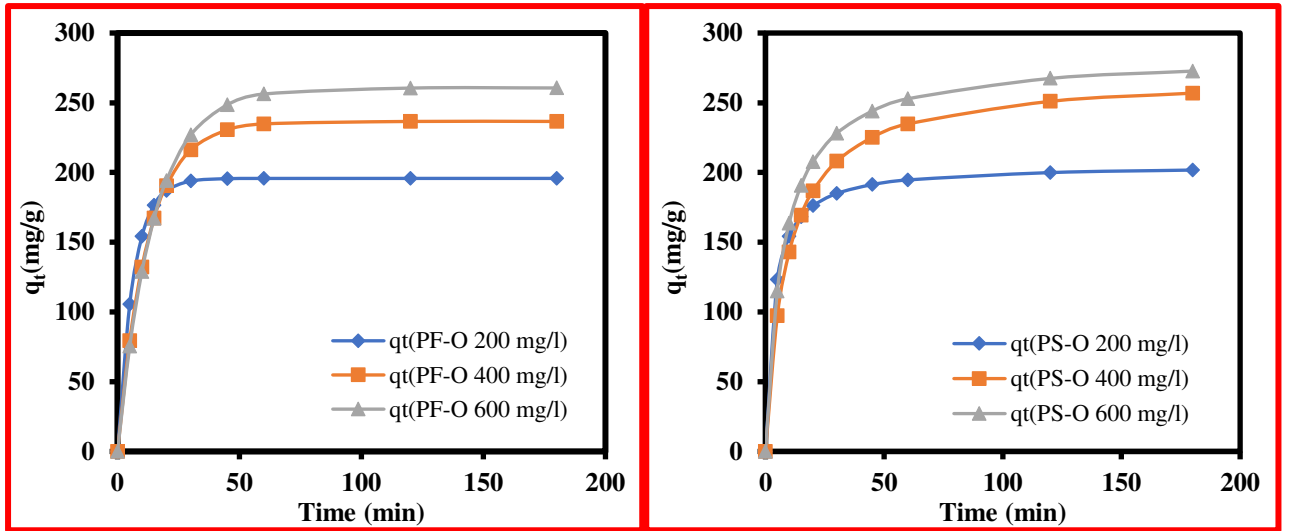
403 **Table 6:** Error-values for kinetic modelling

Pseudo-first order	Pseudo-second order	Elovich	Bangham	Intra-particle diffusion
200 mg/L				
ARE = 0.717	ARE = 0.381	ARE = 0.991	ARE = 0.224	ARE = 0.302
APE = 7.966	APE = 4.244	APE = 11.013	APE = 2.493	APE = 3.357
EABS = 115.729	EABS = 60.948	EABS = 172.162	EABS = 39.338	EABS = 57.578
ERRSQ = 3006.291	ERRSQ = 915.453	ERRSQ = 5968.522	ERRSQ = 269.545	ERRSQ = 798.796
Hybrid = 19.433	Hybrid = 5.959	Hybrid = 34.194	Hybrid = 1.526	Hybrid = 4.103
MPSD = 0.126	MPSD = 0.039	MPSD = 0.201	MPSD = 0.009	MPSD = 0.021
X ² = 23.164	X ² = 6.540	X ² = 37.727	X ² = 1.580	X ² = 4.290
SNE = 1.0556	SNE = 1.0853	SNE = 1.0429	SNE = 1.1676	SNE = 1.0872
400 mg/L				
ARE = 0.640	ARE = 0.478	ARE = 0.641	ARE = 0.418	ARE = 2.256
APE = 7.117	APE = 5.322	APE = 7.118	APE = 4.648	APE = 25.072
EABS = 98.498	EABS = 72.640	EABS = 128.429	EABS = 69.708	EABS = 444.425
ERRSQ = 2094.604	ERRSQ = 1534.557	ERRSQ = 2758.988	ERRSQ = 1206.422	ERRSQ = 38727.5
Hybrid = 14.619	Hybrid = 11.040	Hybrid = 13.857	Hybrid = 7.874	Hybrid = 170.500
MPSD = 0.111	MPSD = 0.081	MPSD = 0.072	MPSD = 0.053	MPSD = 0.807
X ² = 14.079	X ² = 9.0132	X ² = 15.143	X ² = 7.045	X ² = 149.164
SNE = 1.0645	SNE = 1.0642	SNE = 1.0599	SNE = 1.0744	SNE = 1.0205
600 mg/L				
ARE = 0.781	ARE = 0.466	ARE = 0.614	ARE = 0.308	ARE = 0.763
APE = 8.676	APE = 5.174	APE = 6.824	APE = 3.422	APE = 8.473
EABS = 124.270	EABS = 81.743	EABS = 131.238	EABS = 59.301	EABS = 158.100
ERRSQ = 4855.067	ERRSQ = 1347.187	ERRSQ = 2375.086	ERRSQ = 1003.834	ERRSQ = 4581.149
Hybrid = 33.572	Hybrid = 7.952	Hybrid = 10.656	Hybrid = 5.527	Hybrid = 21.520
MPSD = 0.238	MPSD = 0.048	MPSD = 0.0512	MPSD = 0.0309	MPSD = 0.110
X ² = 53.369	X ² = 7.561	X ² = 11.003	X ² = 4.968	X ² = 22.673
SNE = 1.0455	SNE = 1.0764	SNE = 1.0675	SNE = 1.0733	SNE = 1.0462

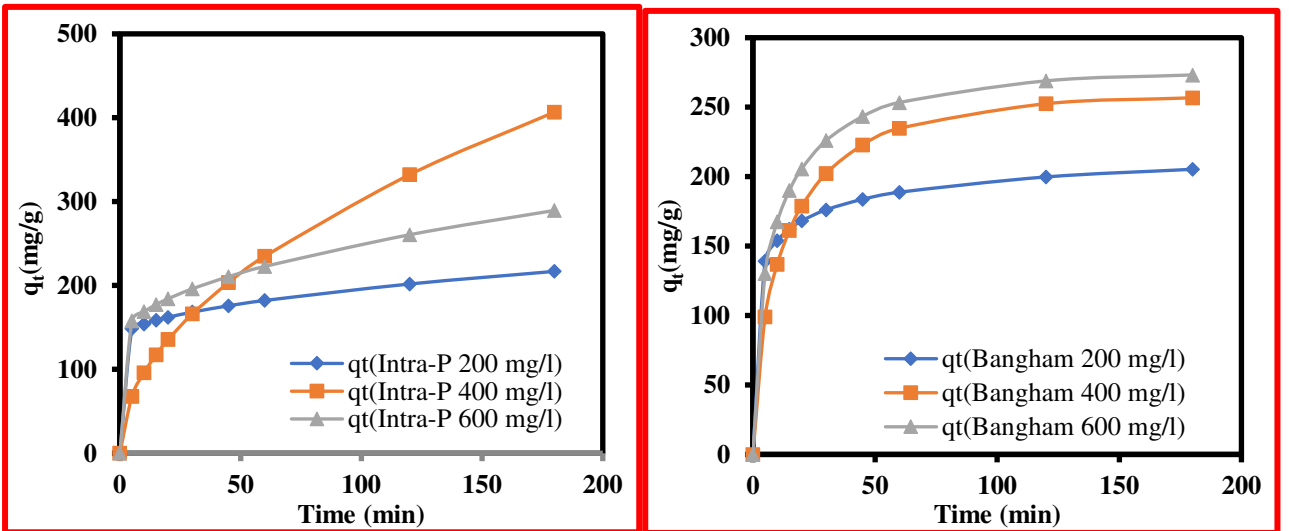
404

405

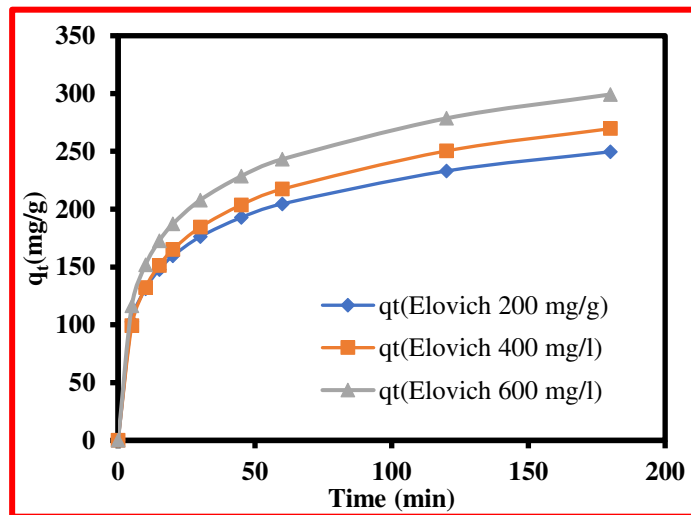
406



407



408



409 **Fig. 8:** The respective kinetic plots for PFO, PSO, Intraparticle diffusion, Elovich and Bangham
410 model

411 **Table 7:** Kinetic model parameters

Pseudo-first order	Pseudo-second order	Elovich	Bangham	Intra-particle diffusion
200 mg/L				
$q_e = 195.755$	$q_e = 205.482$	$\alpha = 100$	$q_e = 226.263$	$k_{id} = 6.118$
$K_1 = 0.155$	$K_2 = 1.4E-03$	$\beta = 0.024$	$k_b = 0.634$	$C = 134.767$
$R^2 = 0.990$	$R^2 = 0.997$	$R^2 = 0.980$	$n = 0.254$	$R^2 = 0.997$
			$R^2 = 0.999$	
400 mg/L				
$q_e = 236.602$	$q_e = 269.533$	$\alpha = 76.389$	$q_e = 258.852$	$k_{id} = 30.317$
$K_1 = 0.0817$	$K_2 = 4.2E-04$	$\beta = 0.021$	$k_b = 0.172$	$C = 0.01$
$R^2 = 0.994$	$R^2 = 0.996$	$R^2 = 0.992$	$n = 0.641$	$R^2 = 0.922$
			$R^2 = 0.997$	
600 mg/L				
$q_e = 260.600$	$q_e = 283.808$	$\alpha = 100.00$	$q_e = 276.077$	$k_{id} = 11.773$
$K_1 = 0.0683$	$K_2 = 4.8E-04$	$\beta = 0.020$	$k_b = 0.264$	$C = 131.564$
$R^2 = 0.988$	$R^2 = 0.997$	$R^2 = 0.994$	$n = 0.549$	$R^2 = 0.988$
			$R^2 = 0.998$	

412

413 3.5. Thermodynamic studies

414 The effect of temperature on the adsorbent-adsorbate interaction during zinc ion uptake is
 415 elucidated by the adsorption thermodynamics parameters (standard free energy, ΔG° , standard
 416 enthalpy, ΔH° and standard entropy, ΔS°). The magnitude and sign convention of these
 417 thermodynamics' parameters are key to explaining the various temperature effects. For
 418 instance, the ΔG° value expresses the feasibility and spontaneity of the adsorption system, the
 419 ΔS° values informs of the degree of disorderliness of the system and the ΔH° value is related
 420 to the heat content and energetic transfer within the adsorption system. The aforementioned
 421 thermodynamics parameters are evaluated accordingly from Eqs. (9) to (10), while Kc is

422 evaluated from Eq. (11) (Igwegbe, Oba, *et al.*, 2020). Where R is the universal gas constant
423 (8.314 J/mol K) and T is the temperature (K).

$$424 \quad \Delta G^\circ = -RT \ln K_c \quad (9)$$

$$425 \quad \Delta G^\circ = \Delta H^\circ - T\Delta S^\circ \quad (10)$$

$$426 \quad K_c = \frac{C_o - C_e}{C_o} \quad (11)$$

427 The parameters presented in Table 8 shows positive ΔG° values and negative ΔS° value, thus
428 implies a non-spontaneous and less energetic nature of the process, respectively. According to
429 Saha *et al.* (2011), such observation suggests the temperature dependence of the 'MA' active
430 sites and underscores the need for the application of external energy to the system. The positive
431 ΔH° values obtained in the study provides further confirmation of the endothermicity of the
432 adsorption process. Also, the relatively large ΔH° value obtained in the study is well within the
433 physicochemical adsorption range and could be related to the strong bond obtainable from the
434 ample carboxylic and carbonyl groups on the 'MA'.

435 **Table 8:** Thermodynamic parameters

Temp. (K)	ΔG° (KJ.mol ⁻¹)	ΔH° (KJ.mol ⁻¹)	ΔS° (JK ⁻¹ .mol ⁻¹)
30	9.276		
50	11.378	61.241	-4.875
60	12.494		

436

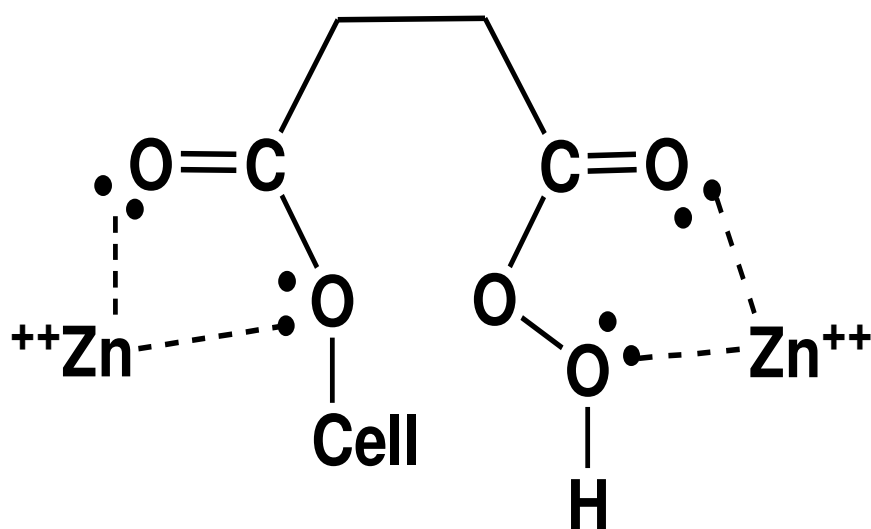
437 3.6. Adsorption mechanism

438 The probable adsorption mechanism involved in the sorption of zinc ion onto 'MA' is discussed
439 as follows;

440 (i) ***ion exchange and electrostatic interaction:*** This interaction resulted mainly from the
441 chemical bonds formed between negatively charged functional groups of the adsorbent and the

442 positively charged Zn (II) ions [see Eqs. (6) & (7)]. This mechanism is predominant when the
443 $\text{pH} > \text{pH}_{\text{PZC}}$. The oxygenous (carboxylate, carbonyl and hydroxyl) surface groups of 'MA' were
444 primarily responsible for the electrostatic interactions at favourable solution pH.

445 (ii) **Electron-donor-acceptor interaction:** Due to the presence of H-donor functional
446 groups ($-\text{OH}$ and $-\text{COOH}$) on 'MA', the mechanism of adsorption could be based on the
447 complexation between the metal ion and the anionic $\text{MA}-\text{COO}^-$ conjugate (H-acceptor)
448 (Scheme 1). Also, the carbonyl groups of 'MA' can engage in donor-acceptor interaction,
449 during which the carbonyl groups of stronger dipole moment could donate the electron which
450 would be accepted by the adsorbate (Mattson *et al.*, 1969).



451

452 **Scheme 1:** Proposed mechanism for zinc ion adsorption onto 'MA'.

453 4. Conclusions

454 A novel biosorbent, with high carboxyl content, was synthesized via the esterification reaction
455 between highly cellulosic Alhagi root material (AG) and succinic acid. The novel biosorbent
456 was effective for aqueous zinc ion uptake. Using different adsorbent characterization tools
457 (SEM, EDX, FTIR and pH_{pzc} analyses) the acidic nature of 'MA' and its textural characteristics
458 was explained. The equilibrium and kinetic modelling suggested a hybrid mix of monolayer-

459 multilayer adsorption and intraparticle diffusion-controlled chemisorption, respectively. The
460 entire sorption process was pH-responsive, while electrostatic and electro-donor-acceptor
461 interaction was established as the major uptake mechanism. Based on experimental findings,
462 'MA' has proven to be an excellent adsorbent for the removal due to the nature of its surface
463 functional groups.

464 **Ethics declarations**

465 *Conflict of interest*

466 The authors declared no potential conflicts of interest concerning the research, authorship,
467 and/or publication of this article.

468 *Ethical approval*

469 This work does not contain any studies with human participants or animals performed by any
470 of the authors. The authors claim compliance with the ethical standards.

471 **References**

- 472 Abdelraheem, W. H., Komy, Z. R., & Ismail, N. M. (2017). Electrochemical determination of
473 Cu^{2+} complexation in the extract of *E. crassipes* by anodic stripping voltammetry.
474 *Arabian Journal of Chemistry*, 10, S1105-S1110.
- 475 Abdelraheem, W. H., Rabia, M. K., & Ismail, N. M. (2016). Evaluation of copper speciation
476 in the extract of *Eichhornia crassipes* using reverse and forward/CLE voltammetric
477 titrations. *Arabian Journal of Chemistry*, 9, S1670-S1678.
- 478 Abonyi, M., Aniagor, C., & Menkiti, M. (2019). Effective Dephenolation of Effluent from
479 Petroleum Industry Using Ionic-Liquid-Induced Hybrid Adsorbent. *Arabian Journal*
480 *for Science and Engineering*, 44(12), 10017-10029.

481 Adigun, O., Oninla, V., & Babarinde, N. A. (2019). Application of sugarcane leaves as biomass
482 in the removal of cadmium (II), lead (II) and zinc (II) ions from polluted water.
483 *International Journal of Energy and Water Resources*, 3(2), 141-152.

484 Ahmad, M. F., Haydar, S., & Quraishi, T. A. (2013). Enhancement of biosorption of zinc ions
485 from aqueous solution by immobilized *Candida utilis* and *Candida tropicalis* cells.
486 *International Biodeterioration & Biodegradation*, 83, 119-128.

487 Al-Shaalan, N. H., Ali, I., ALothman, Z. A., Al-Wahaibi, L. H., & Alabdulmonem, H. (2019).
488 High performance removal and simulation studies of diuron pesticide in water on
489 MWCNTs. *Journal of Molecular Liquids*, 289, 111039.

490 Ali, I., Alharbi, O. M., ALothman, Z. A., Alwarthan, A., & Al-Mohaimed, A. M. (2019).
491 Preparation of a carboxymethylcellulose-iron composite for uptake of atorvastatin in
492 water. *International journal of biological macromolecules*, 132, 244-253.

493 Ali, I., Alharbi, O. M., Alothman, Z. A., & Badjah, A. Y. (2018). Kinetics, thermodynamics,
494 and modeling of amido black dye photodegradation in water using Co/TiO₂
495 nanoparticles. *Photochemistry and photobiology*, 94(5), 935-941.

496 Aniagor, C., & Menkiti, M. (2018). Kinetics and mechanistic description of adsorptive uptake
497 of crystal violet dye by lignified elephant grass complexed isolate. *Journal of*
498 *Environmental Chemical Engineering*, 6(2), 2105-2118.

499 Aniagor, C., & Menkiti, M. (2019). Synthesis, modification and use of lignified bamboo isolate
500 for the renovation of crystal violet dye effluent. *Applied Water Science*, 9(4), 77.

501 Aniagor, C. O., Igwegbe, C. A., Ighalo, J. O., & Oba, S. N. (2021). Adsorption of doxycycline
502 from aqueous media: A review. *Journal of Molecular Liquids*, 116124.
503 doi:<https://doi.org/10.1016/j.molliq.2021.116124>

504 ANIAGOR, C. O., & MENKITI, M. C. (2020). RELATIONAL DESCRIPTION OF AN
505 ADSORPTION SYSTEM BASED ON ISOTHERM, ADSORPTION DENSITY,

506 ADSORPTION POTENTIAL, HOPPING NUMBER AND SURFACE COVERAGE.
507 *Sigma*, 38(3), 1073-1098.

508 Awual, M. R. (2016). Solid phase sensitive palladium (II) ions detection and recovery using
509 ligand based efficient conjugate nanomaterials. *Chemical Engineering Journal*, 300,
510 264-272.

511 Awual, M. R., Alharthi, N. H., Hasan, M. M., Karim, M. R., Islam, A., Znad, H., Hossain, M.
512 A., Halim, M. E., Rahman, M. M., & Khaleque, M. A. (2017). Inorganic-organic based
513 novel nano-conjugate material for effective cobalt (II) ions capturing from wastewater.
514 *Chemical Engineering Journal*, 324, 130-139.

515 Awual, M. R., Hasan, M. M., Asiri, A. M., & Rahman, M. M. (2019). Novel optical composite
516 material for efficient vanadium (III) capturing from wastewater. *Journal of Molecular*
517 *Liquids*, 283, 704-712.

518 Awual, M. R., Hasan, M. M., Islam, A., Rahman, M. M., Asiri, A. M., Khaleque, M. A., &
519 Sheikh, M. C. (2019). Offering an innovative composited material for effective lead (II)
520 monitoring and removal from polluted water. *Journal of Cleaner Production*, 231, 214-
521 223.

522 Badruddoza, A. Z. M., Shawon, Z. B. Z., Tay, W. J. D., Hidajat, K., & Uddin, M. S. (2013).
523 Fe₃O₄/cyclodextrin polymer nanocomposites for selective heavy metals removal from
524 industrial wastewater. *Carbohydrate polymers*, 91(1), 322-332.

525 Barakat, M. (2011). New trends in removing heavy metals from industrial wastewater. *Arabian*
526 *Journal of Chemistry*, 4(4), 361-377.

527 Chen, X., Lv, F., Lin, Y., Wang, Z., Meng, L., Zhang, Q., Zhang, W., & Li, L. (2018). Structure
528 evolution of polyethylene-plasticizer film at industrially relevant conditions studied by
529 in-situ X-ray scattering: The role of crystal stress. *European Polymer Journal*, 101,
530 358-367.

531 Dada, A., Olalekan, A., Olatunya, A., & Dada, O. (2012). Langmuir, Freundlich, Temkin and
532 Dubinin–Radushkevich isotherms studies of equilibrium sorption of Zn²⁺ unto
533 phosphoric acid modified rice husk. *IOSR Journal of Applied Chemistry*, 3(1), 38-45.

534 Delgado, N., Capparelli, A., Navarro, A., & Marino, D. (2019). Pharmaceutical emerging
535 pollutants removal from water using powdered activated carbon: study of kinetics and
536 adsorption equilibrium. *Journal of environmental management*, 236, 301-308.

537 Ebrahimi, A., Ehteshami, M., & Dahrazma, B. (2015). Isotherm and kinetic studies for the
538 biosorption of cadmium from aqueous solution by Alhaji maurorum seed. *Process
539 Safety and Environmental Protection*, 98, 374-382.

540 Foo, K. Y., & Hameed, B. H. (2010). Insights into the modeling of adsorption isotherm
541 systems. *Chemical Engineering Journal*, 156(1), 2-10.

542 Freundlich, H. (1907). Über die adsorption in lösungen. *Zeitschrift für physikalische Chemie*,
543 57(1), 385-470.

544 Guo, X., & Wang, J. (2019). A general kinetic model for adsorption: theoretical analysis and
545 modeling. *Journal of Molecular Liquids*, 288, 111100.

546 Hashem, A., Al-Anwar, A., Nagy, N. M., Hussein, D. M., & Eisa, S. (2016). Isotherms and
547 kinetic studies on adsorption of Hg (II) ions onto Ziziphus spina-christi L. from aqueous
548 solutions. *Green Processing and Synthesis*, 5(2), 213-224.

549 Hashem, A., Aniagor, C., Hussein, D., & Farag, S. (2021). Application of novel butane-1, 4-
550 dioic acid-functionalized cellulosic biosorbent for aqueous cobalt ion sequestration.
551 *Cellulose*, 1-17.

552 Hashem, A., ANIAGOR, C. O., Nasr, M., & Abou-Okeil, A. (2021). Efficacy of treated sodium
553 alginate and activated carbon fibre for Pb(II) adsorption. *International journal of
554 biological macromolecules*, 1-16. doi:<https://doi.org/10.1016/j.ijbiomac.2021.02.067>

555 Hashem, A., Badawy, S., Farag, S., Mohamed, L., Fletcher, A., & Taha, G. (2020). Non-linear
556 adsorption characteristics of modified pine wood sawdust optimised for adsorption of
557 Cd (II) from aqueous systems. *Journal of Environmental Chemical Engineering*,
558 103966.

559 Hashem, A., & Badawy, S. M. (2015). *Sesbania sesban* L. biomass as a novel adsorbent for
560 removal of Pb (II) ions from aqueous solution: non-linear and error analysis. *Green*
561 *Processing and Synthesis*, 4(3), 179-190.

562 Hashem, A., Fletcher, A., Younis, H., Mauof, H., & Abou-Okeil, A. (2020). Adsorption of Pb
563 (II) ions from contaminated water by 1, 2, 3, 4-butanetetracarboxylic acid-modified
564 microcrystalline cellulose: Isotherms, kinetics, and thermodynamic studies.
565 *International journal of biological macromolecules*, 164, 3193-3203.

566 Hashem, A., Hussein, H. A., Sanousy, M. A., Adam, E., & Saad, E. E. (2011).
567 Monomethylolated thiourea–sawdust as a new adsorbent for removal of Hg (II) from
568 contaminated water: equilibrium kinetic and thermodynamic studies. *Polymer-Plastics*
569 *Technology and Engineering*, 50(12), 1220-1230.

570 Hashem, A., Nasr, M., Fletcher, A., & Mohamed, L. A. (2020). Aminated acrylic fabric waste
571 derived sorbent for Cd (II) ion removal from aqueous solutions: mechanism, equilibria
572 and kinetics. *Journal of Polymers and the Environment*, 1-12.

573 Ighalo, J. O., Tijani, I. O., Ajala, J., Ayandele, F. O., Eletta, O., & Adeniyi, A. G. (2020).
574 Competitive Biosorption of Pb (II) and Cu (II) by Functionalised *Micropogonias*
575 *undulatus* Scales. *Recent Innovations in Chemical Engineering*, 13, 1-12.

576 Igwegbe, C. A., Oba, S. N., Aniagor, C. O., Adeniyi, A. G., & Ighalo, J. O. (2020). Adsorption
577 of ciprofloxacin from water: a comprehensive review. *Journal of Industrial and*
578 *Engineering Chemistry*.

579 Igwegbe, C. A., Onukwuli, O. D., Ighalo, J. O., & Okoye, P. U. (2020). Adsorption of cationic
580 dyes on Dacryodes edulis seeds activated carbon modified using phosphoric acid and
581 sodium chloride. *Environmental Processes*, 7(4), 1151-1171.

582 Jagaba, A., Kutty, S., Khaw, S., Lai, C., Isa, M., Baloo, L., Lawal, I., Abubakar, S., Umaru, I.,
583 & Zango, Z. (2020). Derived hybrid biosorbent for zinc (II) removal from aqueous
584 solution by continuous-flow activated sludge system. *Journal of Water Process
585 Engineering*, 34, 101152.

586 Kapoor, A., & Yang, R. (1989). Correlation of equilibrium adsorption data of condensable
587 vapours on porous adsorbents. *Gas Separation & Purification*, 3(4), 187-192.

588 Khair, U., Fahmi, H., Al Hakim, S., & Rahim, R. (2017). *Forecasting error calculation with
589 mean absolute deviation and mean absolute percentage error*. Paper presented at the
590 Journal of Physics: Conference Series.

591 Khalil, M., Hashem, A., & Hebeish, A. (1990). Carboxymethylation of maize starch. *Starch-
592 Stärke*, 42(2), 60-63.

593 Khan, A., Ataullah, R., & Al-Haddad, A. (1997). Equilibrium adsorption studies of some
594 aromatic pollutants from dilute aqueous solutions on activated carbon at different
595 temperatures. *Journal of colloid and interface science*, 194(1), 154-165.

596 King, P., Anuradha, K., Lahari, S. B., Kumar, Y. P., & Prasad, V. (2008). Biosorption of zinc
597 from aqueous solution using *Azadirachta indica* bark: equilibrium and kinetic studies.
598 *J Hazard Mater*, 152(1), 324-329.

599 Komy, Z. R., Abdelraheem, W. H., & Ismail, N. M. (2013). Biosorption of Cu²⁺ by *Eichhornia
600 crassipes*: Physicochemical characterization, biosorption modeling and mechanism.
601 *Journal of King Saud University-Science*, 25(1), 47-56.

602 Kumar, K. V., Porkodi, K., & Rocha, F. (2008). Comparison of various error functions in
603 predicting the optimum isotherm by linear and non-linear regression analysis for the
604 sorption of basic red 9 by activated carbon. *J Hazard Mater*, 150(1), 158-165.

605 Langmuir, I. (1916). The constitution and fundamental properties of solids and liquids. Part I.
606 Solids. *Journal of the American chemical society*, 38(11), 2221-2295.

607 Liu, X., Chen, Z.-Q., Han, B., Su, C.-L., Han, Q., & Chen, W.-Z. (2018). Biosorption of copper
608 ions from aqueous solution using rape straw powders: optimization, equilibrium and
609 kinetic studies. *Ecotoxicology and Environmental Safety*, 150, 251-259.

610 Luef, E., Prey, T., & Kubicek, C. P. (1991). Biosorption of zinc by fungal mycelial wastes.
611 *Applied Microbiology and biotechnology*, 34(5), 688-692.

612 Marquardt, D. W. (1963). An algorithm for least-squares estimation of nonlinear parameters.
613 *Journal of the society for Industrial and Applied Mathematics*, 11(2), 431-441.

614 Matouq, M., Jildeh, N., Qtaishat, M., Hindiye, M., & Al Syouf, M. Q. (2015). The adsorption
615 kinetics and modeling for heavy metals removal from wastewater by Moringa pods.
616 *Journal of Environmental Chemical Engineering*, 3(2), 775-784.

617 Mattson, J. A., Mark Jr, H. B., Malbin, M. D., Weber Jr, W. J., & Crittenden, J. C. (1969).
618 Surface chemistry of active carbon: specific adsorption of phenols. *Journal of colloid
619 and interface science*, 31(1), 116-130.

620 Menkiti, M., Abonyi, M., & Aniagor, C. (2018). Process Equilibrium, Kinetics, and
621 Mechanisms of Ionic-Liquid Induced Dephenolation of Petroleum Effluent. *Water
622 Conservation Science and Engineering*, 3(3), 205-220.

623 Menkiti, M., & Aniagor, C. (2018). Parametric studies on descriptive isotherms for the uptake
624 of crystal violet dye from aqueous solution onto lignin-rich adsorbent. *Arabian Journal
625 for Science and Engineering*, 43(5), 2375-2392.

626 Menkiti, M., Aniagor, C., Agu, C., & Ugonabo, V. (2018). Effective adsorption of crystal violet
627 dye from an aqueous solution using lignin-rich isolate from elephant grass. *Water*
628 *Conservation Science and Engineering*, 3(1), 33-46.

629 Ng, J., Cheung, W., & McKay, G. (2002). Equilibrium studies of the sorption of Cu (II) ions
630 onto chitosan. *Journal of colloid and interface science*, 255(1), 64-74.

631 Noh, J. S., & Schwarz, J. A. (1990). Effect of HNO₃ treatment on the surface acidity of
632 activated carbons. *Carbon*, 28(5), 675-682.

633 Oba, S. N., Ighalo, J. O., Aniagor, C. O., & Igwegbe, C. A. (2021). Removal of ibuprofen from
634 aqueous media by adsorption: A comprehensive review. *Science of the total*
635 *environment*, 146608. doi:<https://doi.org/10.1016/j.scitotenv.2021.146608>

636 Paduraru, C., Tofan, L., Teodosiu, C., Bunia, I., Tudorachi, N., & Toma, O. (2015). Biosorption
637 of zinc (II) on rapeseed waste: equilibrium studies and thermogravimetric
638 investigations. *Process Safety and Environmental Protection*, 94, 18-28.

639 Redlich, O., & Peterson, D. L. (1959). A useful adsorption isotherm. *Journal of physical*
640 *chemistry*, 63(6), 1024-1024.

641 Rivas, F., Beltrán, F., Gimeno, O., Frades, J., & Carvalho, F. (2006). Adsorption of landfill
642 leachates onto activated carbon: equilibrium and kinetics. *J Hazard Mater*, 131(1-3),
643 170-178.

644 Saha, P., & Chowdhury, S. (2011). Insight into adsorption thermodynamics. *Thermodynamics*,
645 16, 349-364.

646 Sasmal, S., Goud, V. V., & Mohanty, K. (2012). Characterization of biomasses available in the
647 region of North-East India for production of biofuels. *Biomass and Bioenergy*, 45, 212-
648 220.

649 Schweitzer, L., & Noblet, J. (2018). *Water Contamination and Pollution*. 261-290.
650 doi:10.1016/b978-0-12-809270-5.00011-x

651 Shahat, A., Hassan, H. M., Azzazy, H. M., El-Sharkawy, E., Abdou, H. M., & Awual, M. R.
652 (2018). Novel hierarchical composite adsorbent for selective lead (II) ions capturing
653 from wastewater samples. *Chemical Engineering Journal*, 332, 377-386.

654 Shahat, A., Hassan, H. M., El-Shahat, M., El Shahawy, O., & Awual, M. R. (2018). Visual
655 nickel (II) ions treatment in petroleum samples using a mesoporous composite
656 adsorbent. *Chemical Engineering Journal*, 334, 957-967.

657 Temkin, M. (1940). Kinetics of ammonia synthesis on promoted iron catalysts. *Acta*
658 *physiochim. URSS*, 12, 327-356.

659 Toth, J. (1971). State equation of the solid-gas interface layers. *Acta chim. hung.*, 69, 311-328.

660 Vargas, A. M., Cazetta, A. L., Martins, A. C., Moraes, J. C., Garcia, E. E., Gauze, G. F., Costa,
661 W. F., & Almeida, V. C. (2012). Kinetic and equilibrium studies: Adsorption of food
662 dyes Acid Yellow 6, Acid Yellow 23, and Acid Red 18 on activated carbon from
663 flamboyant pods. *Chemical Engineering Journal*, 181, 243-250.

664 Wang, G., Chang, Q., Zhang, M., & Han, X. (2013). Effect of pH on the removal of Cr (III)
665 and Cr (VI) from aqueous solution by modified polyethyleneimine. *Reactive and*
666 *Functional Polymers*, 73(11), 1439-1446.

667 Wang, L., Shi, C., Pan, L., Zhang, X., & Zou, J.-J. (2020). Rational design, synthesis,
668 adsorption principles and applications of metal oxide adsorbents: a review. *Nanoscale*,
669 12(8), 4790-4815.

670 Wang, X. S., Qin, Y., & Li, Z. F. (2006). Biosorption of zinc from aqueous solutions by rice
671 bran: kinetics and equilibrium studies. *Separation science and technology*, 41(4), 747-
672 756.

673 Wołowiec, M., Komorowska-Kaufman, M., Pruss, A., Rzepa, G., & Bajda, T. (2019). Removal
674 of heavy metals and metalloids from water using drinking water treatment residuals as
675 adsorbents: A review. *Minerals*, 9(8), 487.

676 Yan, Y., Xu, X., Shi, C., Yan, W., Zhang, L., & Wang, G. (2019). Ecotoxicological effects and
677 accumulation of ciprofloxacin in *Eichhornia crassipes* under hydroponic conditions.
678 *Environ Sci Pollut Res Int*, 26(29), 30348-30355. doi:10.1007/s11356-019-06232-5
679 Zhuang, S., & Wang, J. (2019). Removal of cobalt ion from aqueous solution using magnetic
680 graphene oxide/chitosan composite. *Environmental Progress & Sustainable Energy*,
681 38(s1), S32-S41.
682 Zhuang, S., Zhu, K., & Wang, J. (2020). Fibrous chitosan/cellulose composite as an efficient
683 adsorbent for Co (II) removal. *Journal of Cleaner Production*, 124911.

684